AUTHOR(S): PENG, Q., SUN, Y., GE, B., FENG, J., GUO, J., FERNANDEZ, C. and HUANG, J.

TITLE: In-situ atomic-scale phase transformation of Mg under hydrogen conditions.

YEAR: 2018

Publisher citation: PENG, Q., SUN, Y., GE, B., FENG, J., GUO, J., FERNANDEZ, C. and HUANG, J. 2018. In-situ atomic-scale phase transformation of Mg under hydrogen conditions. Journal of physical chemistry C [online], 122(34), pages 19532-19539. Available from: https://doi.org/10.1021/acs.jpcc.8b04694

OpenAIR citation: PENG, Q., SUN, Y., GE, B., FENG, J., GUO, J., FERNANDEZ, C. and HUANG, J. [2018]. In-situ atomic-scale phase transformation of Mg under hydrogen conditions. Journal of physical chemistry C, 122(34), pages 19532-19539. Held on OpenAIR [online]. Available from: https://openair.rgu.ac.uk/

THE JOURNAL OF PHYSICAL CHEMISTRY C

C: Surfaces, Interfaces, Porous Materials, and Catalysis

In-Situ Atomic-Scale Phase Transformation of Mg Under Hydrogen Conditions

Qiuming Peng, Yong Sun, Bingcheng Ge, Jiawen Feng, Jianxin Guo, Carlos Fernandez, and Jianyu Huang

J. Phys. Chem. C, **Just Accepted Manuscript** • DOI: 10.1021/acs.jpcc.8b04694 • Publication Date (Web): 09 Aug 2018

In-Situ Atomic-Scale Phase Transformation of Mg under Hydrogen Conditions

Qiuming Peng[*,1], *Yong Sun*[1], *Bingcheng Ge*[1], *Jiawen Feng*[1], *Jianxin Guo*[*,2], *Carlos Fernandez*[3], *Jianyu Huang*[1]

[1] *State Key Laboratory of Metastable Materials Science and Technology, Yanshan University, Qinhuangdao, 066004, PR. China.*

[2]*Hebei Provincial Key Lab of Optoelectronic Information Materials, College of Physics Science and Technology, Hebei University, Baoding, 071002, PR China*

[3]*School of Pharmacy and life sciences, Rober Gordon University, Aberdeen, AB107GJ, UK*

Abstract

Magnesium hydrogenation issue poses a serious obstacle to designing strong and reliable structural materials, as well as offering a safe alternative for hydrogen applications. Understanding phase transformation of magnesium under hydrogen gas plays an essential role in developing high performance structural materials and hydrogen storage materials. Herein, we report *in-situ* atomic-scale observations of phase transformation of Mg and Mg-1wt.%Pd alloy under hydrogen conditions in an aberration-corrected environmental transmission electron microscopy. Compare with magnesium hydrogenation reaction, magnesium oxidation reaction predominately occurs at room temperature even under pure hydrogen gas (99.9%). In comparison, magnesium hydrogenation is readily detected in the interface between Mg and Mg_6Pd, due to catalytic role of Mg_6Pd. Note that the nanoscale MgH_2 compound transfers into MgO spontaneously, and the interface strain remarkably varies during phase transformation. These atomic-level observations and calculations provide fundamental knowledge to elucidate the issue of magnesium hydrogenation.

Keywords: Magnesium; Hydride; Growth; Phase transformation

Introduction

Mg-based alloys play essential roles in developing new structural and functional materials owing to their high specific strength and large gravimetric hydrogen density.[1] However, both structural and functional materials are closely related to the subject of Mg hydrogenation. In the case of Mg-based structural materials, the hydrogen gas affects mechanical properties, lead to premature or catastrophic failure.[2] Many mechanisms have been proposed to explain this phenomenon in the past decades in terms of macro-scale experiments.[3] For example, it proposes that interstitial H atoms aggregate on the cleavage plane ahead of a crack, and dislocation emission becomes easier.[4] In addition, it also believes that some hydrides form during preparing process, and change deformation mode, resulting in crack blunting and defeats cleavage-like fracture.[5] However, the detailed mechanism on the interactive roles between Mg and H remains unclear, especially on the atomic-level.

In addition, the pulverization of Mg-based storage hydrogen materials has been confirmed as one of main reasons for the invalidation of ab/desorption hydrogen cycles.[6] The structure morphology and phase stability of MgH_2 medium are associated with the storage-hydrogen properties of Mg-based materials, in which the formation and decomposition of MgH_2 lead to the large inertial stress due to different lattice parameters in the interface of MgH_2 and Mg.[7, 8] Basically, it has been confirmed that the hydrogenation behavior of Mg-based storage-hydrogen materials is related to the formation and decomposition of MgH_2.[9] However, the formation process and phase transformation of MgH_2 on the atomic-level has hardly reported owing to technique challenges.

Undoubtedly, Mg hydrogenation plays an essential role in elucidating service performances of Mg alloys in the fields of both structural and functional materials. Atomic-level observation and atomistic simulations/calculations are desirable to clarify these scientific phenomena. To resolve atomic-scale dynamic hydrogenation process, *in-situ* environmental transmission electron microscopy (ETEM) that has

evolved dramatically in recent years [10-12]offers the capability for temperature-, time-, and pressure-resolved imaging of gas-surface reactions by introducing a reactive gas to the sample while simultaneously monitoring the structural evolution. Theoretical calculations using first principles density function theory (DFT) provides other evidences to elucidate these processes.[13]

In present work, we disclose the hydrogenation behaviors of pure Mg and Mg-1wt%Pd alloy under pure hydrogen gas (99.9%) by performing *in-situ* ETEM technique. The formation processes of MgO and MgH_2 combined with phase stability of MgH_2 were firstly detected on the atomic-scale level. Meanwhile, the transformation mechanisms have been elucidated based on DFT calculations.

Results and discussion

In-situ oxidation of Mg under hydrogen condition

Typically, a high purity Mg ingot has been prepared by the chill-casting method[14]. The Mg slice was prepared by a common preparing process via diamond-cutting and ion beam milling. The oxidation reaction of the Mg slice occurred in the grain boundary under a hydrogen gas environment of 1.0 ~ 1.1 mbar (**Figure 1a and Movie S1**). The oxidation reaction of Mg at the grain boundary is contradictory with expectations in the field-Mg hydrogenation reaction under pure hydrogenation.[15] There are two possible reasons for the origin of oxygen atoms. On one hand, the sample adsorbed oxygen during the transformation of sample. On the other hand, the impurity of hydrogen gas involves oxygen although the purity of hydrogen gas is high. Taking into account of a low Pilling-Bedworth ratio (~0.8), the formed MgO film is incompact owing to the lower crystal spacing of MgO in contrast to that of Mg[16-18]. In this regard, the oxidation process can occur although the existence of MgO. Thus, the oxygenation behaviour under ETEM observation is mainly related to oxygen impurity in pure hydrogen gas.

The phase compositions and orientation relationship (ORs) between Mg and MgO have been confirmed by high revolution transmission electron microscopy (**HRTEM,**

Figure 1b) and selected electron area diffraction (**SEAD, Figure 1c**). Their ORs are $(01\bar{1}0)_{Mg}||(020)_{MgO}$ and $[2\bar{1}\bar{1}0]_{Mg}||[001]_{MgO,}$ $(0002)_{Mg}||(200)_{MgO}$ and $[2\bar{1}\bar{1}0]_{Mg}||[001]_{MgO}$, respectively. Time-lapse images (**Figure 2**) revealed that the MgO was preferential to form in the grain boundaries with retarding reaction time. The e-beam-induced temperature increase of the sample was estimated to be less than 1 ^{o}C[19]. In contrast, these ORs are different from those observed in the high-temperature oxidation, i.e., $(11\bar{2}0)_{Mg}||(220)_{MgO}$ and $[2\bar{1}\bar{1}0]_{Mg}||[001]_{MgO,}$[20] and the low-temperature confined growth of MgO, i.e., $(0002)_{Mg}||(110)_{MgO}$ and $[2\bar{1}\bar{1}0]_{Mg}||$ $[001]_{MgO}$.[21] In addition, the MgO layers were observed to be crystalline, and epitaxial, and consistent with an early, incomplete phase of oxide formation(Al_2O_3 [22] and FeO [23]). Finally, the *in-situ* observations show that Morie fingers formed at the initial oxidation, and then the epitaxial MgO/Mg interface become incoherent. The incoherency stress due to the lattice mismatch between Mg and MgO relaxes partly,[24] resulting in a large tilt angle of ~20.1^{o} along MgO (020) plane near the MgO/Mg interface. In this regard, it can be confirmed that the Mg hydrogenation can hardly occur except for presenting effective catalysts or prohibiting oxidation.

***In-situ* hydrogenation of Mg near to Mg_6Pd compound**

To probe the hydrogenation process of Mg, a Mg-1wt.%Pd alloy has been prepared by ultrahigh pressure melting technique (UPM, 4 GPa and 1300 ^{o}C). A typical equiaxial morphology has been detected in the UPMed Mg-1wt.%Pd alloy. Some fine Mg_6Pd eutectic phases with an average dimension of ~30 nm are confirmed in terms of X-ray diffraction pattern (XRD, **Figure 3a**) and transmission electron microscopy (TEM) images (**Figure 3b and Figure 3c**). The high resolution transmission electron microscopy (HRTEM) image (**Figure 3d**) along [001] electron beam direction indicates that the spacing values of (660) and (600) are 0.254 nm and 0.352 nm, respectively. Both of them are consistent with those of perfect Mg_6Pd compound (JCPDF No. 25-1084)

A typical hydrogenation process of Mg has been detected near to Mg_6Pd particles under the same hydrogen gas environment of 1.0 ~ 1.1 mbar (**Movie S2**). During the

reaction process, time-lapse images reveal a new phase presents in the junction of Mg_6Pd (**Figure 4**). The HRTEM image (**Figure 5a and Figure 5b**) show the d spacing of new phase value is ~ 2.26 nm, corresponding to the (200) plane of MgH_2. In addition, the crystal orientation relationship has been confirmed between MgH_2 and Mg_6Pd: $(002)_{MgH2}//(310)_{Mg6Pd}$ (**Figure 5c**), suggesting the formation of MgH_2 is closely relative to Mg_6Pd. After phase transformation, the Mg_5Pd_2 phase is identified by the HRTEM (**Figure 6a,**) and fast fourier transform (FFT) images (**Figure 6 b**). The possible decomposition reaction can be shown as followed: $2Mg_6Pd \rightarrow Mg_5Pd_2 + 2Mg$, which is consistent with the phase diagram.[25] The electron energy loss spectroscopy (EELS, **Figure 6c**) shows that some new peaks at 14.9, 22.6 and 57.5 eV, which correspond to MgH_2 (14.8 eV)[26] and MgO (22.8 and 57.8 eV)[27], respectively, are detected except for the primitive Mg_6Pd peaks (10.5, 21.3, 31.8, 52.7 and 70 eV). These results are consistent with those observed by *in-situ* SEAD patters (**Figure 6d**).

To clarify the coexistent phenomena of MgO and MgH_2 in the hydrogenation process of Mg-1wt%Pd alloy, *in-situ* structure transformation in the interface of MgO/MgH_2 has been observed (**Figure 7 and Movie S3**). The HRTEM (**Figure 8a**) and fast fourier transform (FFT) images (**Figure 8b**) demonstrates that the ORs are $(020)_{MgH2}//(020)_{MgO}$ and $[001]_{MgH2}/[110]_{MgO}$, respectively. With increasing reaction time, time-lapse images show that the volume fraction of MgH_2 reduces, and the amount of MgO increases correspondingly. It demonstrates that the phase transformation from MgH_2 to MgO occurs spontaneously, resulting in the coexistence of both MgH_2 to MgO. The result agrees well with oxidation reaction of Mg even under hydrogenation gas.

Phase transformation mechanisms

To understand the hydrogenation and oxidation mechanisms, first principles calculations were performed to obtain the formation energies (E_f) of MgH_2, MgO and the phase transformation from MgH_2 to MgO. The E_f values of MgH_2 and MgO are 3.55 eV and 4.52 eV, respectively. It suggests that it is prior to form MgO instead of MgH_2, which is the main reason for the preferential product of MgO under pure

hydrogen gas pressure. In contrast, MgH_2 readily forms at the Mg/Mg_6Pd interface (**Figure 9a**). The formation of the MgH_2 at the Mg/Mg6Pd interface is attributed to the catalytic role of the Pd compound and its decomposition.[28]

To probe this spontaneous phase transformation from MgH_2 to MgO under hydrogen conditions, the transformation process has been elucidated in terms of the first principles calculations. The results show that the dissociation energy (originating from the energy of the chemical reaction $MgH_2 \rightarrow Mg+H_2$) is 3.139 eV/H_2 (**Figure 9b**) when H atoms break away from MgH_2 to form H_2 molecule. Comparatively, the formation of MgO releases the energy of -5.032 eV/MgO (originating from the energy of the chemical reaction $2Mg+O_2 \rightarrow 2MgO$). The energy barrier of removing next H atoms layer from MgH_2 is 2.264 eV/H_2 (**Figure 9c**). And then the MgO layer (**Figure 9d**) shifts displace to combine with MgH_2 (**Figure 9e**). It can decrease the energy of 0.581 eV/MgO. Actually, the above steps occur simultaneously, and the total energy reduces by -0.207 eV, demonstrating that the transformation from MgH_2 to MgO is spontaneous (**Figure 9f**). In addition, the continuous phase transformation processes (**Figure 9g and Movie S4**) exhibit this transformation is not only a spontaneous reaction (-0.207 eV for the surface transformation), but also an accelerated process (-1.420 eV for the 7th layer transformation).

The surface energies of MgH_2 on different surfaces show that MgH_2 (001) surface is the most stable (**Figure 10**), which is consistent with HRTEM. The surface energies at HRTEM lead us to believe the oxygen atoms undergo ingress along the MgH_2 [001] direction. The lattice mismatch between MgH_2 and MgO (Table 1) suggests MgH_2 (001)/MgO(001) interface is possible. The smallest lattice misfits of MgH_2 (001) and MgO along (001) surface are 5.7% and 6.1%, respectively. With increasing the number of MgO layers, the strain of MgH_2 increases, but the strain of MgO decreases (**Table 2**).

Summary

In-situ ETEM observations combining DFT calculations have been performed to

investigate two main chemical reactions of Mg: hydrogenation and oxidation processes. The results reveal the oxidation reaction plays a crucial role in tuning phase transformation of Mg even under hydrogen environments. In addition, with the presence of Mg_6Pd catalyst, MgH_2 compound is prone to form in the interface of Mg/Mg_6Pd. However, the MgH_2 compound will spontaneously change to MgO with retarding time. The DFT calculation of the MgO oxide formation energy is consistent with the facile oxidation of Mg. The observations on two processes extend the understanding on the fundamental characteristics of Mg-based materials.

Methods

Specimen preparation

High purity Mg (>99.9%) ingot was melted at 720 ^{o}C for 1h, and then directly solidified by chill-casting method[14]. The cooling rate was below 0.5 mm/s to achieve the bar of 50 mm in diameter with a large grain size (~ 5 mm). The grain orientation along $[10\bar{1}0]$ direction was confirmed by electron back scattered diffraction equipped with a HKL-EBSD system.

High purity Mg and Pd (99.99 wt%) powders were utilized to synthesis Mg-1wt.%Pd alloy by ultrahigh pressure method. The detailed process has been elucidated in our previous results.[2] Specifically, the pressure and temperature were 4 GPa and 1300 ^{o}C, respectively. The dimensions were a diameter of 10 mm and a length of 14 mm. After ultrahigh pressure treatment, the samples were quenched to room temperature directly before unloading pressure.

Microstructural characterization

The microstructural investigations were performed using SEM observation. The sample was prepared by a procedure involving grinding up to 2400 SiC paper, followed by mechanical polishing with 9, 3, and 1 μm water-free diamond suspensions and final polishing using 0.05 μm colloidal silica. The final step included chemical polishing in a fresh solution containing a mixture of 100 mL of methanol, 12 mL of hydrochloric acid, and 8 mL of nitric acid. XRD was

carried out on the Rigatu D/MAX/2500/PC with Cu Kα radiation at a scan from 20° to 80° with a step of 0.02 and a scan rate of 4° min^{-1}. Both Mg and Mg-1w.%Pd slices were prepared by diamond cutting, and thin foil specimens of 3 mm in diameter were punched from the slices for TEM observation. The specimens were prepared by traditional mechanical grinding and polishing from 500 to 30 μm in thickness, then ion-beam milling using Gatan PIPS 691 with 4 keV.

First-principles density function theory (DFT) calculation

All calculations are performed using Vienna ab initio simulation package (VASP [29]) based on density functional theory (DFT), and the ion-electron interaction described with the projector augmented wave (PAW) method.[30] The generalized gradient approximation (GGA) by the Perdew, Burke, and Ernaerhof (PBE[31]) form is used to describe the exchange-correlation functions. Cutoff energy of the plane wave basis is set to 520 eV. The ions are relaxed toward equilibrium until the Hellmann-Feynman forces are less than 10^{-5} eV/Å. Brillouin zone integrations with a Gaussian broadening of 0.05 eV are performed. The tetragonal structure of α-MgH_2 (space group: P42/mnm) and the NaCl-structure MgO (space group: Fm-3m) are used as the calculation models in our work. The centered Monkhorst Pack k-point mesh for sampling the Brillouin zone was 20×20 ×20 for MgH_2 and MgO bulks, 20×20×1 for (001), (100), (101) and (110) surface of Mg and Mg (001) / MgO (001) interface, respectively. The electronic structures including density of states (DOS[32]) was obtained using k point of 30×30×1 Gamma centered Monkhorst-Pack k-point grid. A large vacuum space of 20 Å was used for avoid any interaction between slabs. All calculations are carried out by structure optimization with relaxation of all atoms.

The formation energies of MgO and MgH_2 are defined as[33]:

$$E_f(MgO) = E_{MgO} - E_{Mg} - E_O \quad (1)$$

$$E_f(MgH_2) = E_{MgH_2} - E_{Mg} - 2E_H \quad (2)$$

where E_{MgO} and E_{MgH_2} are the total energy of the MgO and MgH_2 bulks, respectively.

E_O and E_H are the total energy of every H and O atom deriving from the total energy of the H_2 and O_2 molecular, respectively. Herein, the oxygen spin polarization was considered.

The surface energy of MgH_2 surface is defined as [34]:

$$\sigma_{MgH_2} = (E_{surface} - nE_{bulk}) / 2S \quad (3)$$

where $E_{surface}$ and E_{bulk} are the total energy of the MgH_2 surfaces including (001), (100), (101) and (110) plane, respectively. To obtain the accurate surface energy, the MgH_2 surfaces contain the certain number atoms which is an integral number of MgH_2 formula units. S is the area of the MgH_2 surface. 1/2 is because of two surfaces every slab.

The formation energy every MgO layer in MgH2 (001) surface is defined as [33]:

$$E_{f(n)} = (E_{MgO(n)/MgH_2} + 2nE_{H_2/2} - E_{MgO(n-1)/MgH_2} - nE_{O_2/2}) / n \quad (4)$$

where $E_{MgO(n)/MgH_2}$ and $E_{MgO(n-1)/MgH_2}$ are the total energy of the MgO/MgH_2 interface with n layer MgO (Figure 9). When n is 1, the equation means the formation energy of one layer MgO in MgH_2 (001) by the introduction of O_2 and the release of H_2. The rest can be done in the same manner. $E_{H_2/2}$ and $E_{O_2/2}$ are the total energy of every H and O atom deriving from the total energy of the H_2 and O_2 molecular, respectively.

ASSOCIATED CONTENT

Supporting Information

The Movies and their descriptions were involved. These material are available free of charge via the Internet at http://pubs.acs.org.

AUTHOR INFORMATION

Corresponding Author

*(Q.M. Peng) E-mail: pengqiuming@gmail.com.

*(J.X. Guo) E-mail: gjx@hbu.edu.cn.

Author Contributions

The manuscript was written through contributions of all authors. All authors have given approval to the final version of the manuscript.

Notes

The authors declare no competing financial interest.

Acknowledgements

We greatly acknowledge the financial support from National Key Research and Development Program (2017YFB0702001), NSFC (51771162), the Natural Science Foundation of Hebei Province (E2017201034), and the High-Performance Computing Platform of Hebei University.

References

(1). Pollock, T. M., Weight loss with magnesium alloys. *Science* **2010**, *328*, 986-987.

(2). Bobby Kannan, M.; Dietzel, W., Pitting-induced hydrogen embrittlement of magnesium–aluminium alloy. *Mater. Design* **2012**, *42*, 321-326.

(3). Koyama, M.; Akiyama, E.; Lee, Y.K.; Raabe, D.; Tsuzaki, K., Overview of hydrogen embrittlement in high-Mn steels. *Int. J. Hydrogen Energy* **2017**, ***42***, 12706-12723.

(4). Nygren, K. E.; Bertsch, K. M.; Wang, S.; Bei, H.; Nagao, A.; Robertson, I. M., Hydrogen embrittlement in compositionally complex FeNiCoCrMn FCC solid solution alloy. *Curr. Opin. Solid State Mater. Sci.* **2018**, *22*, 1-7.

(5). Venezuela, J.; Blanch, J.; Zulkiply, A.; Liu, Q.; Zhou, Q.; Zhang, M.; Atrens, A., Further study of the hydrogen embrittlement of martensitic advanced high-strength steel in simulated auto service conditions. *Corr. Sci.* **2018**, *135*, 120-135.

(6). Pistidda, C.; Bergemann, N.; Wurr, J.; Rzeszutek, A.; Møller, K.; Hansen, B.; Garroni, S.; Horstmann, C.; Milanese, C.; Girella, A.; *et.al,* Hydrogen storage systems from waste Mg alloys. *J. Power Sources* **2014**, *270*, 554-563.

(7). Zhang, J.; Yan, S.; Qu, H., Stress/strain effects on thermodynamic properties of magnesium hydride: A brief review. *Int. J. Hydrogen Energy* **2017**, *42*,

16603-16610.

(8). Matović, L.; Kurko, S.; Rašković-Lovre, Ž.; Vujasin, R.; Milanović, I.; Milošević, S.; Grbović Novaković, J., Assessment of changes in desorption mechanism of MgH_2 after ion bombardment induced destabilization. *Int. J. Hydrogen Energy* **2012**, *37*, 6727-6732.

(9). Wan, Q.; Li, P.; Shan, J.; Zhai, F.; Li, Z.; Qu, X., Superior catalytic effect of nickel ferrite nanoparticles in improving hydrogen storage properties of MgH_2. *J. Phys. Chem. C* **2015**, *119*, 2925-2934.

(10). Yue, Y.; Yuchi, D.; Guan, P.; Xu, J.; Guo, L.; Liu, J., Atomic scale observation of oxygen delivery during silver–oxygen nanoparticle catalysed oxidation of carbon nanotubes. *Nat. Commun.* **2016**, *7*, 12251.

(11). Mildner, S.; Beleggia, M.; Mierwaldt, D.; Hansen, T. W.; Wagner, J. B.; Yazdi, S.; Kasama, T.; Ciston, J.; Zhu, Y.; Jooss, C., Environmental TEM study of electron beam induced electrochemistry of Pr0.64Ca0.36MnO3 catalysts for oxygen evolution. *J. Phys. Chem. C* **2015**, *119*, 5301-5310.

(12). Koh, A. L.; Gidcumb, E.; Zhou, O.; Sinclair, R., Observations of carbon nanotube oxidation in an aberration-corrected environmental transmission electron microscope. *ACS Nano* **2013**, *7*, 2566-2572.

(13). Zhou, G.; Luo, L.; Li, L.; Ciston, J.; Stach, E. A.; Yang, J. C., Step-edge-induced oxide growth during the oxidation of Cu surfaces. *Phys .Rev. Lett.* **2012**, *109,* 235502.

(14). Peng, Q.; Huang, Y.; Zhou, L.; Hort, N.; Kainer, K. U., Preparation and properties of high purity Mg–Y biomaterials. *Biomaterials* **2010**, *31*, 398-403.

(15). Li, L.; Peng, B.; Ji, W.; Chen, J., Studies on the hydrogen storage of magnesium manowires by density gunctional theory. *J. Phys. Chem. C* **2009**, *113*, 3007-3013.

(16). Goonewardene, A. U.; Karunamuni, J.; Kurtz, R. L.; Stockbauer, R. L., An STM study of the oxidation of Mg(0001). *Surf. Sci.***2002**, *501*, 102-111.

(17). Hayden, B. E.; Schweizer, E.; Kötz, R.; Bradshaw, A. M., The early stages of oxidation of magnesium single crystal surfaces. *Surf. Sci.* **1981**, *111*, 26-38.

(18). Francis, M. F.; Taylor, C. D., First-principles insights into the structure of the incipient magnesium oxide and its instability to decomposition: Oxygen chemisorption to Mg(0001) and thermodynamic stability. *Phys. Rev.B* **2013**, *87*, 075450.

(19). Zheng, H.; Liu, Y.; Cao, F.; Wu, S.; Jia, S.; Cao, A.; Zhao, D.; Wang, J., Electron beam-assisted healing of nanopores in magnesium alloys. *Sci. Reports* **2013**, *3*, 1920.

(20). Kooi, B. J.; Palasantzas, G.; Hosson, J. T. M. D., Gas-phase synthesis of magnesium nanoparticles: A high-resolution transmission electron microscopy study. *Appl. Phys. Lett.* **2006**, *89*, 161914.

(21). Zheng, H.; Wu, S.; Sheng, H.; Liu, C.; Liu, Y.; Cao, F.; Zhou, Z.; Zhao, X.; Zhao, D.; Wang, J., Direct atomic-scale observation of layer-by-layer oxide growth during magnesium oxidation. *Appl. Phys. Lett.* **2014**, *104*, 141906.

(22). Brune, J. W., Trost, J., Ertl, G., Interaction of oxygen with Al(111) studied by scanning tunneling microscopy. *J. Chem. Phys.***1993**, *99*, 2128-2148.

(23). Sundararajan, J. A.; Kaur, M.; Qiang, Y., Mechanism of electron beam induced oxide layer thickening on iron–iron oxide core–shell nanoparticles. *J. Phys. Chem. C* **2015**, *119*, 8357-8363.

(24). Bain, J. A.; Chyung, L. J.; Brennan, S.; Clemens, B. M., Elastic strains and coherency stresses in Mo/Ni multilayers. *Phys. Rev. B* **1991**, *44*, 1184-1192.

(25). Smallman, R. E.; Ngan, A. H. W., Modern physical metallurgy, Butterworth-Heinemann: Oxford, **2014**.

(26). Paik, B.; Jones, I. P.; Walton, A.; Mann, V.; Book, D.; Harris, I. R., $MgH_2 \rightarrow Mg$ phase transformation driven by a high-energy electron beam: An *in situ* transmission electron microscopy study. *Philoso. Mag. Lett.* **2010**, *90*, 1-7.

(27). Schaffner, M. H.; Patthey, F.; Schneider, W. D.; Pettersson, L. G. M., Electron energy loss spectroscopy (EELS) of thermally evaporated Cu deposited on MgO(100)/Mo(100). *Surf. Sci.* **1998**, *402-404*, 450-453.

(28). T., R. M.; Elke, W., Phosphane-free palladium-catalyzed coupling reactions: The decisive role of Pd nanoparticles. *Angew. Chem. Int. Ed.***2000**, *39*, 165-168.

(29). Kresse, G.; Furthmüller, J., Efficient iterative schemes for *ab initio* total-energy calculations using a plane-wave basis set. *Phys. Rev. B* **1996**, *54*, 11169-11186.

(30). Blöchl, P. E., Projector augmented-wave method. *Phys. Rev. B* **1994**, *50*, 17953-17979.

(31). Perdew, J. P.; Burke, K.; Ernzerhof, M., Generalized gradient approximation made simple. *Phys. Rev. Lett.* **1996**, *77*, 3865-3868.

(32). Becke, A. D.; Edgecombe, K. E., A simple measure of electron localization in atomic and molecular systems. *J. Chem. Phys.* **1990**, *92*, 5397-5403.

(33). Zhou, Z.; Shi, J.; Guo, L., A comparative study on structural and electronic properties and formation energy of bulk α-Fe_2O_3 using first-principles calculations with different density functionals. *Comput. Mater. Sci.* **2016**, *113*, 117-122.

(34). Aghemenloh, E.; Yusuf, S.; Idiodi, J. O. A., Surface energy calculation of hcp metals using the analytical equivalent crystal theory. *Mater. Chem. Phys.* **2013**, *138*, 529-534.

TOC

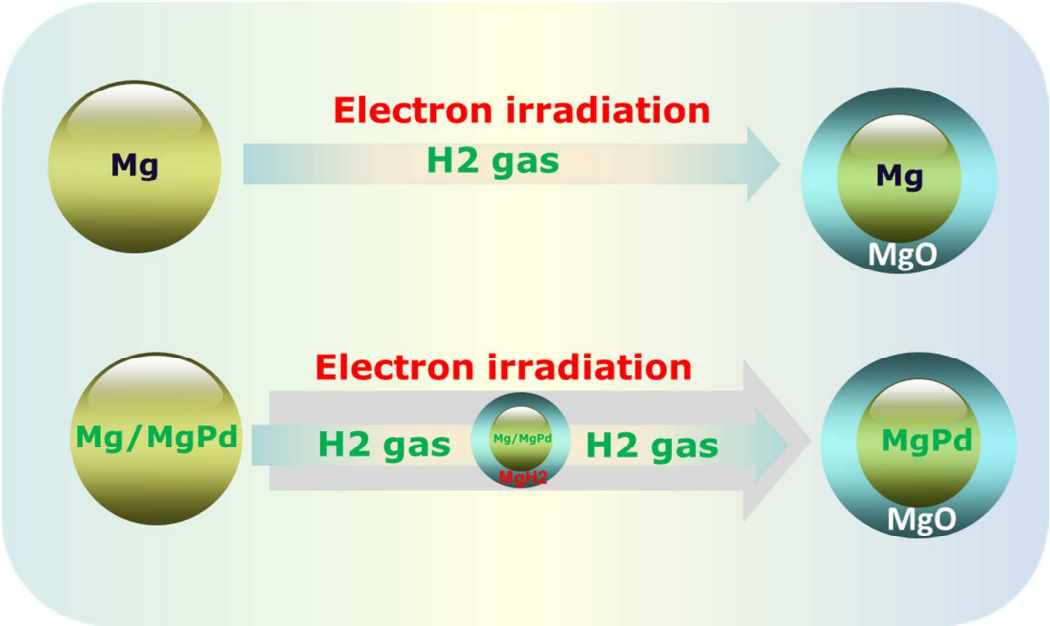
Mg
Electron irradiation
H2 gas
Mg
MgO
Mg/MgPd
Electron irradiation
H2 gas
Mg/MgPd
MgH2
H2 gas
MgPd
MgO

Table 1. Lattice parameters of MgH_2 and MgO.

	a (nm)	b (nm)	c (nm)
MgO	0.424	0.424	0.424
MgH_2	0.450	0.450	0.301

Table 2. The lattice parameters of MgO/MgH_2 system and the strains of MgO and MgH_2 with different numbers of MgO layer.

Layer number of MgO	a (nm)	Strain of MgH_2 (%)	Strain of MgO (%)
1	0.448	0.00	-
2	0.433	-3.37	3.49
3	0.430	-4.13	2.68
4	0.426	-4.87	1.89
5	0.423	-5.49	1.22
6	0.422	-5.83	0.86
7	0.421	-6.03	0.65

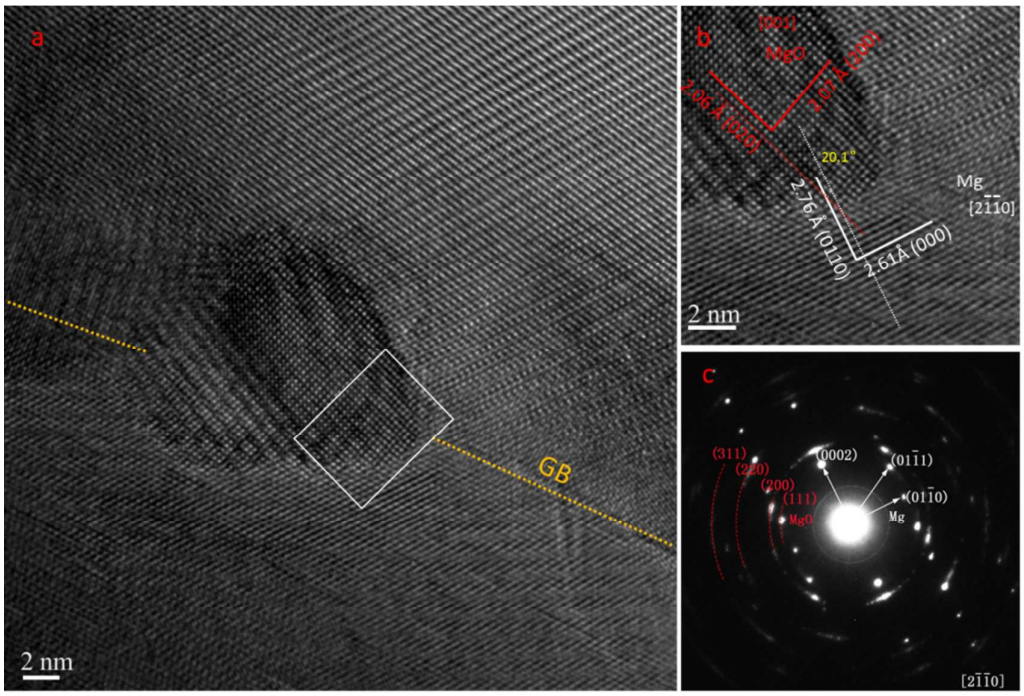

Figure 1. The formation of MgO of pure Mg under hydrogen condition. (**a**), A typical HRTEM image showing the presence of MgO in the grain boundaries of Mg.. (**b**) Local high magnification image of the MgO/Mg interface, wherein the orientation relationships ($(020)_{MgO}//(0110)_{Mg}$, $(200)_{MgO}//(0002)_{Mg}$) are confirmed. A distorted angle of ~20.1^{o} is related to the lattice strain. (**c**) FFT of the MgO/Mg interface. The scatted rings and regular dots correspond to MgO and Mg, respectively, confirming the orientation relationship between Mg and MgO.

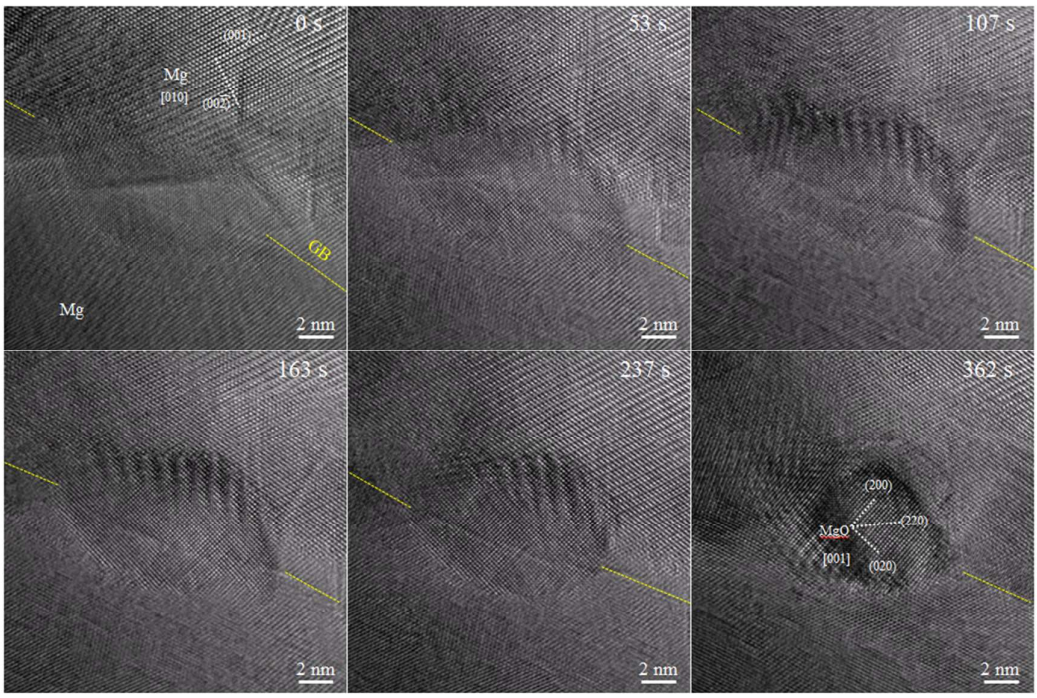

Figure 2. Time-lapse images of phase transformation from Mg to MgO. The yellow dashed-line area shows the grain boundaries of Mg.

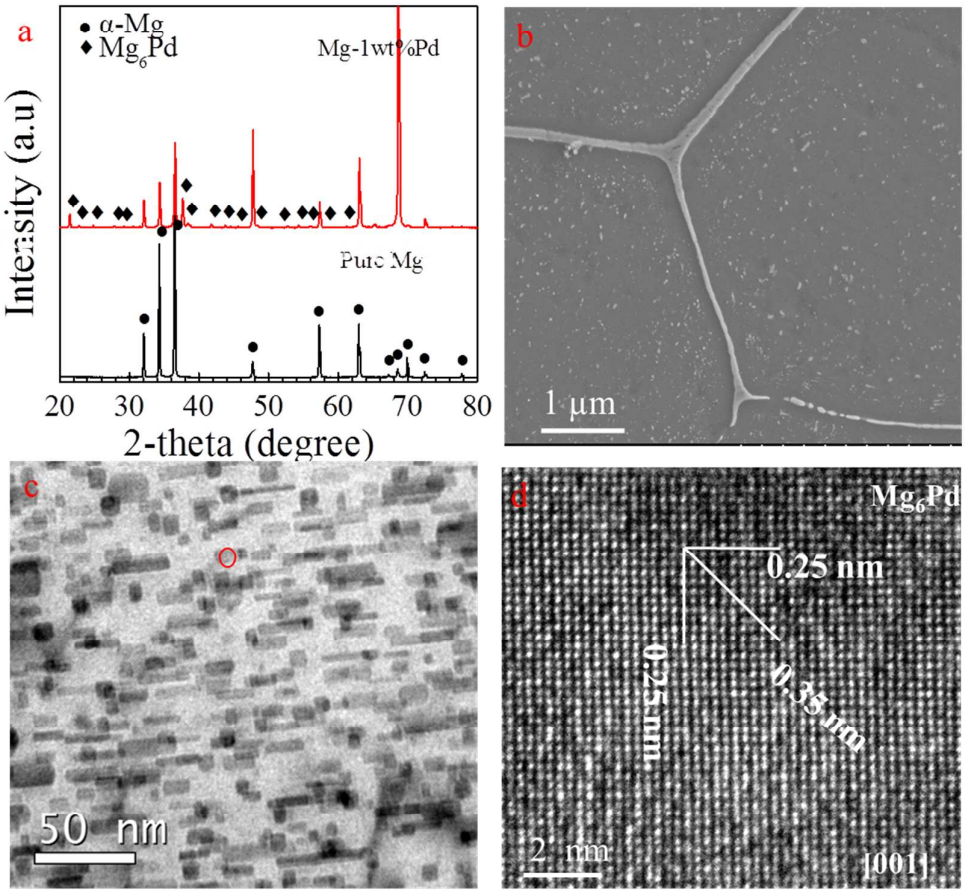

Figure 3: (**a**) XRD patterns of pure Mg and the ultrahigh pressure Mg-1wt%Pd alloy (4GPa, 1300°C). (**b**) SEM image of the ultrahigh pressure Mg-1wt.%Pd alloy. The eutectic Mg_6Pd phases are distributed in both grain boundaries and grain interior. (**c**) TEM image of the ultrahigh pressure Mg-1wt.%Pd alloy. (**d**) HRTEM image of the Mg_6Pd compound along [001] electron beam direction.

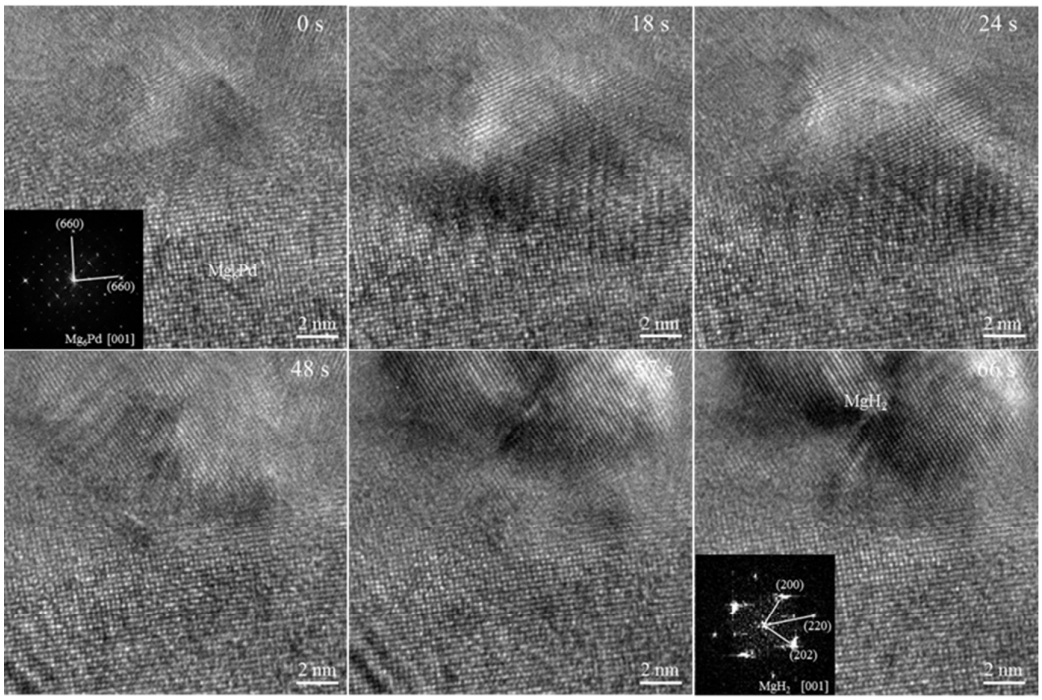

Figure 4. Time-lapse images of phase transformation from Mg to MgH_2 near to the Mg_6Pd particles. The inset images in 0 *s*and 66 *s* corresponds to the SEAD patterns of Mg_6Pd and MgH_2 along [001] direction, respectively.

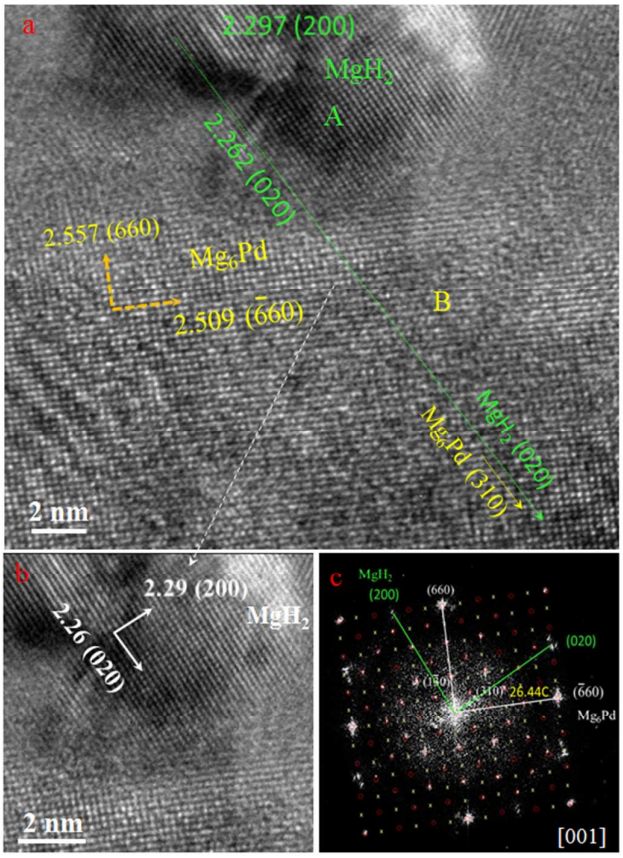

Figure 5. The formation of nano-scale MgH_2 phases. (**a**) The presence of some nano-scale MgH_2 phases near to the Mg_6Pd particles. (**b**) HRTEM image of MgH_2. (**c**) SEAD pattern of the MgH_2/Mg_6Pd interface.

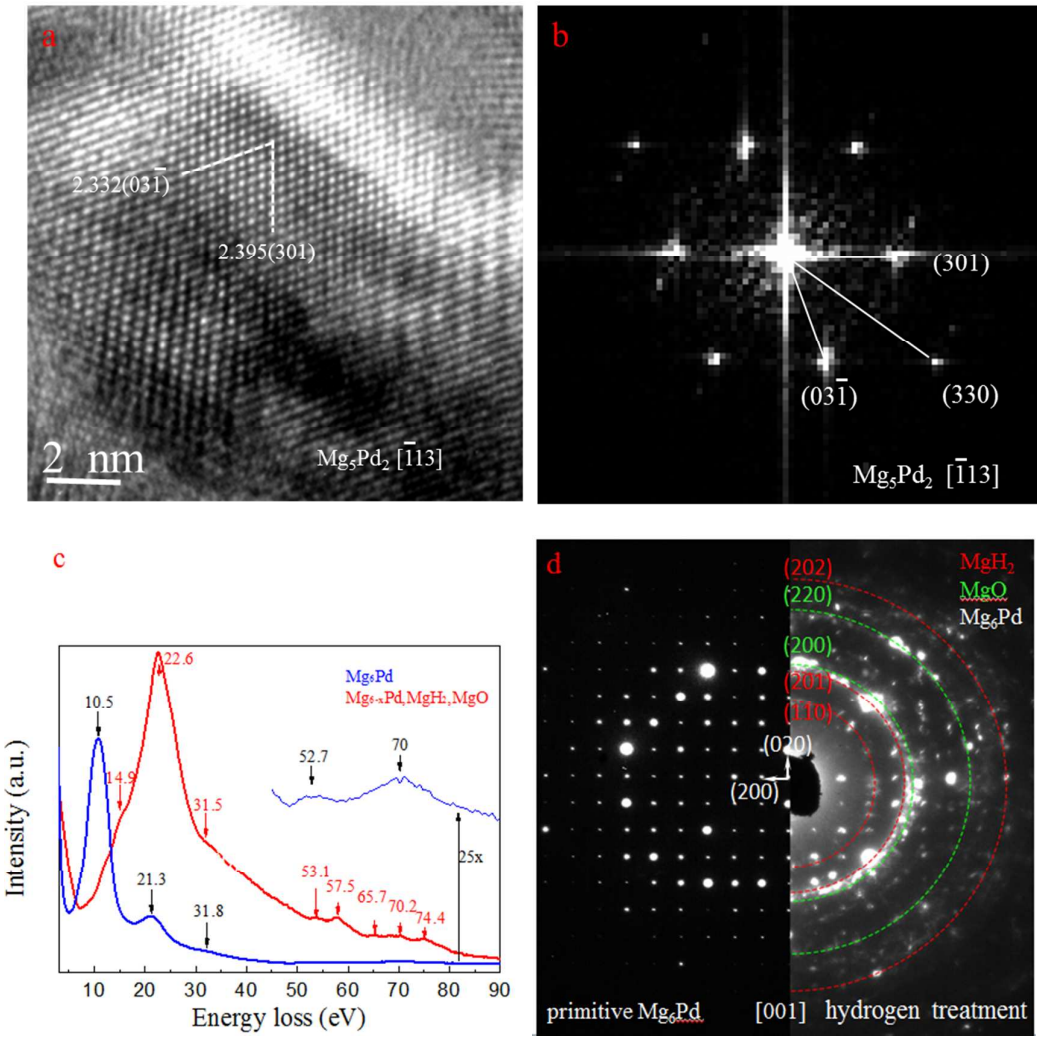

Figure 6. (a) HRTEM image of the Mg_5Pd_2 compound along [-113]. (b) FFT pattern of the Mg6Pd compound dependent on (a). (c) EELS profiles of positions A (red line) and B (blue line) in Figure 4a. (d) Comparison of SEAD patterns of position A after hydrogen treatment in Figure 4a.

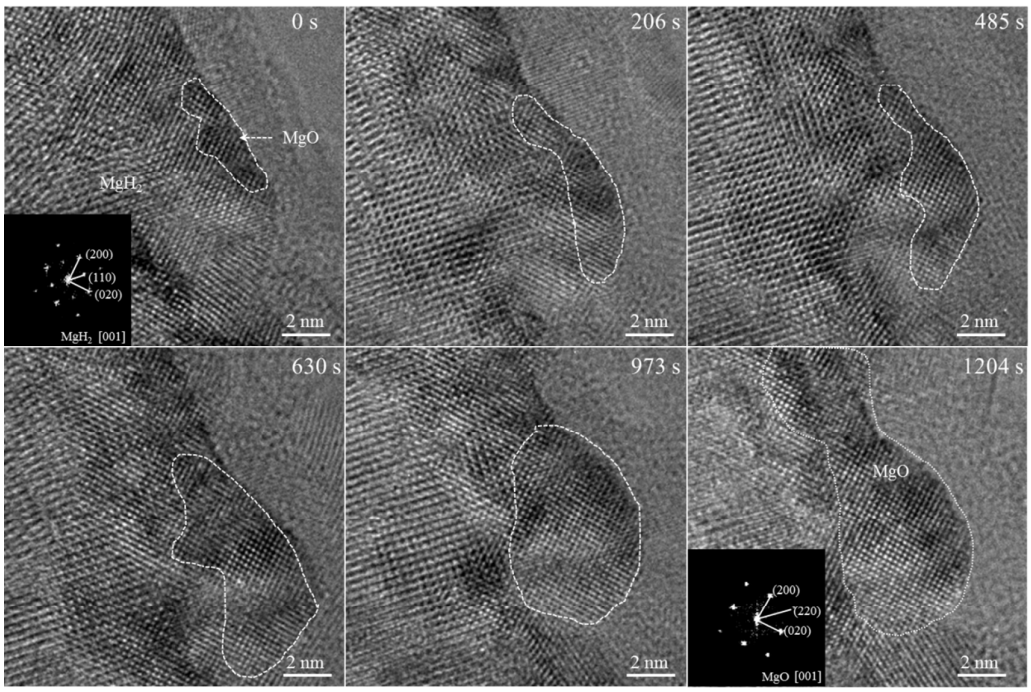

Figure 7. Time-lapse images of phase transformation from MgH_2 to MgO. The dashed-line area shows the boundary of MgO. The inset images in 0 *s* and 1204 *s* corresponds to the SEAD patterns of MgH_2 and MgO along [001] electron beam direction, respectively.

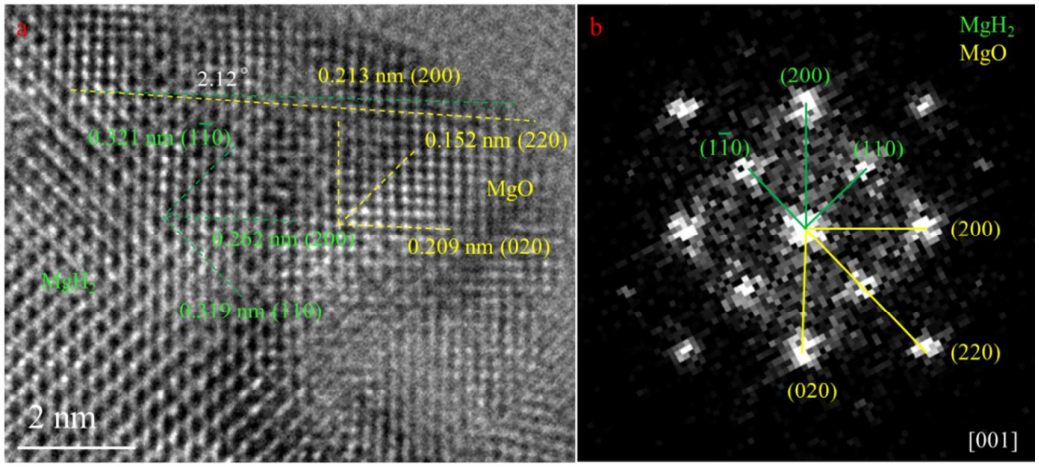

Figure 8. (a) The HRTEM image containing MgH_2 and MgO. (**b**) FFT patterns of MgH_2 and MgO along [001] direction, respectively.

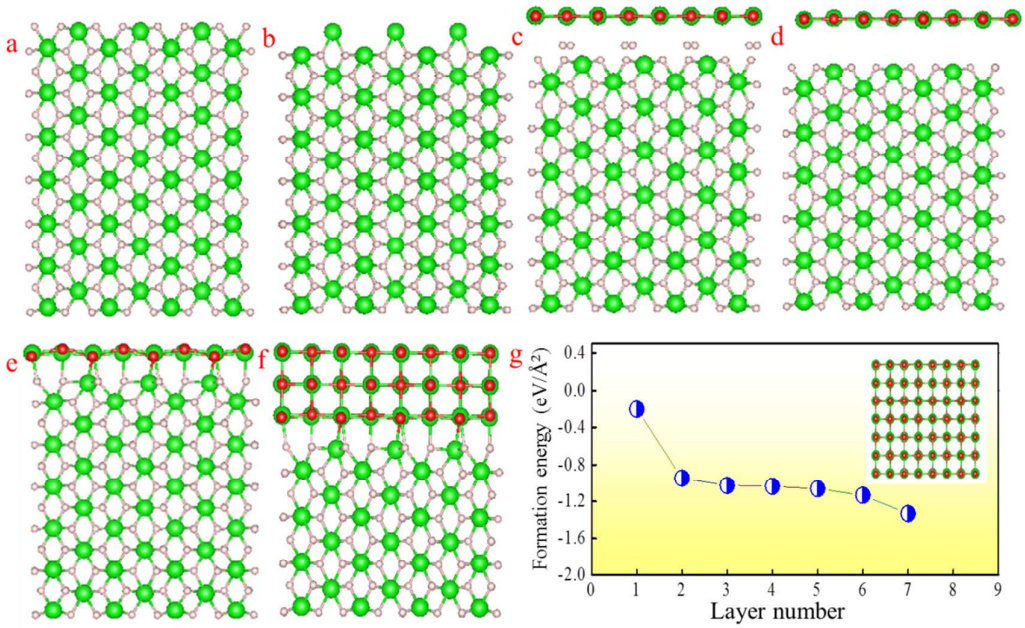

Figure 9. Phase transformation mechanism. (a-f) Time-lapse images of atomic structure evolution of MgH_2 viewed along (001) direction. It reveals that there exists a high stress in the interface of MgH_2/MgO. (g) The formation energy dependent on the layer number of MgO. The presence of MgO leads to the reduction of formation energy, accelerating phase transformation.

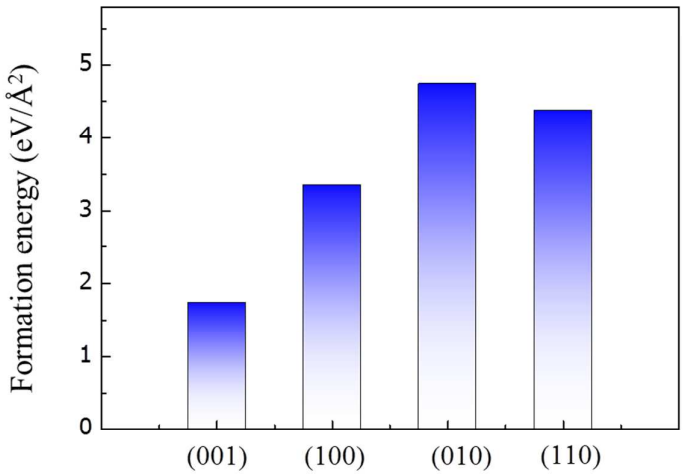

Figure 10: The surface energy of MgH_2 compound in terms of DFT calculations.